Revision 1

Reexamination of the structure of opal-A: A combined study of synchrotron X-ray diffraction and pair distribution function analysis

Seungyeol Lee[1,2,3], Huifang Xu[1,*], and Hongwu Xu[4]

[1]Department of Geoscience, University of Wisconsin–Madison, Madison, WI 53706, USA

[2]USRA Lunar and Planetary Institute, 3600 Bay Area Boulevard, Houston, TX 77058, USA

[3]ARES, NASA Johnson Space Center, 2101 NASA Parkway, Houston, TX 77058, USA

[4]Earth and Environmental Sciences Division, Los Alamos National Laboratory, NM 87545, USA

* Corresponding author:

Prof. Huifang Xu

Department of Geoscience, University of Wisconsin-Madison

1215 West Dayton Street, A352 Weeks Hall Madison, Wisconsin 53706, USA

Tel: 1-608-265-5887

Email: hfxu@geology.wisc.edu

ABSTRACT

The structure of opal-A was not fully understood due to its poorly crystalline nature. To better understand its structural characteristics, we have analyzed opal-AN (amorphous-network) and opal-AG (amorphous-gel) using synchrotron X-ray diffraction (XRD), pair-distribution function (PDF) analysis, and transmission electron microscopy (TEM). Opal-AN mainly exists as an aggregation of different sizes of nanospheres (< 5 nm) generating banded features, whereas opal-AG displays close-packed silica nanospheres with a diameter of ~400 nm. TEM energy-dispersive X-ray spectroscopy (EDS) indicates that Na, Al, K, and Ca are present as trace elements in opal-AN and opal-AG. XRD patterns of both samples show one prominent peak at ~4.0 Å, together with broad peaks at ~2.0 Å, ~1.45 Å, and ~1.2 Å. Previous studies only identified the ~4.0 Å diffraction peak for the definition of opal-A. Hence, opal-A needs to be redefined taking into account the newly observed three broad peaks. PDF patterns of opal-AN and opal-AG reveal short-range atomic pairs (< 15 Å) with almost identical profiles. Both phases exhibit Si-O correlation at 1.61 Å and O-O correlation at 2.64 Å in their [SiO_4] tetrahedra. The currently accepted opal structure is disordered intergrowths of cristobalite- and tridymite-like domains consisting of six-membered rings of [SiO_4] tetrahedra. Our PDF analyses have identified additional, coesite-like nanodomains comprising four-membered [SiO_4] rings. Moreover, we have identified 8-membered rings that can be generated by twinning and stacking faults from six-membered rings. The coesite nanodomains in opal-A may be a precursor for coesite micro-crystals formed by the impact of supersonic micro-projectiles at low-pressures. More broadly, our study has also demonstrated that the combined approach of synchrotron XRD/PDF with TEM is a powerful approach to determine the structures of poorly crystallized minerals.

Keywords: Synchrotron X-ray diffraction, Pair distribution function analysis, Transmission electron microscopy, Local structure, Opal-A.

INTRODUCTION

Opal is a mineral term for amorphous and paracrystalline hydrated silica species that occur commonly in vesicles, veins, and fissures of young rocks (e.g., sandstone, chalk deposits, limonite, geodes, and rhyolite) with environments ranging from deep ocean to terrestrial (Chester and Elderfield 1968; Jones and Segnit 1971; Mortlock and Froelich 1989; Gaillou et al. 2008a). The formation of opal is associated with weathering of silicic rocks, hydrothermal activity, devitrification, diagenetic alteration, and biogenetic processes (Raman and Jayaraman 1953; Jones and Segnit 1971; Gaillou et al. 2008a; Curtis et al. 2019). Opal has been recognized as an indicator for silica diagenesis and paleoclimate changes (Rice et al. 1995; Ragueneau et al. 2000; Clarke 2003; Gaillou et al. 2008a; Murray et al. 2012). Throughout human history, due to their exotic optical properties, certain opals have been widely used as a gemstone in jewelry and decorative arts (Sanders 1964; Darragh et al. 1976; Pewkliang et al. 2008). Recently, opal was observed in the Gale crater on Mars by Curiosity rover's instruments and in Martian meteorites, providing valuable information on Mars' ancient aqueous environment (Lee et al. 2015; Rapin et al. 2018; Sun and Milliken 2018).

Gemologically, opals can be divided into three categories: precious, common, and hyalite, based on whether they display a play-of-color from the diffraction of visible light (Sanders 1964; Sanders 1980). Mineralogically, based on their X-ray diffraction (XRD) patterns, opals are classified into three groups: opal-A, opal-CT, and opal-C (Jones and Segnit 1971; Elzea

et al. 1994). The notations of "C" and "T" refer to cristobalite and tridymite, respectively, owing to the similarity of their XRD patterns (though the peaks are much weaker and more broad) to those of α-cristobalite and α-tridymite. Opal-A (amorphous) is further divided into opal-AG ("amorphous-gel", or closely packed amorphous silica spheres) and opal-AN ("amorphous-network", or hyalite). Opal-AN or hyalite typically has botryoidal morphology and glass-like texture, whereas opal-AG consists of mono- or polydisperse spheres of hydrated silica (Sanders 1980; Curtis et al. 2019). The ordered arrangement of certain sizes of silica spheres (~1500 to ~3500 Å in diameter) causes the play-of-color seen in precious opal (Sanders 1964; Darragh et al. 1976).

Despite the importance of opals in geological and gemological applications, their structures remain largely unresolved because their XRD patterns are characterized by broad and weak peaks, suggesting short- and medium-range ordered structures (Wilson 2014; Curtis et al. 2019). Other techniques such as Raman spectroscopy, nuclear magnetic resonance (NMR) spectroscopy, infra-red (IR) spectroscopy and neutron scattering have been attempted to unravel the structures of opals. Small-angle neutron scattering (SANS) was employed to measure the range of sizes of the silica spheres (Graetsch and Ibel 1997). IR spectroscopic analyses of natural opals suggest that water is present in various forms: trapped water molecules, surface-adsorbed water, and free and hydrogen-bonded silanol (Si-OH) groups on the surfaces (Day and Jones 2008; Boboň et al. 2011). ^{29}Si NMR spectroscopic measurements also indicate the presence of silanol groups, and ^{27}Al NMR spectra reveal partial replacement of Si by Al in opal [SiO_4] tetrahedra (Brown et al. 2003; Paris et al. 2007). Raman spectroscopic measurements suggest that the medium-range ordered structure of opal is closer to the atomic framework of tridymite than to that of cristobalite (Ilieva et al. 2007). However, these spectroscopic techniques are not

suitable for resolving medium-range structural features of opals; some studies did not even distinguish different types of opals (e.g., opal-A, opal-CT and opal-C), causing confusion.

The goal of this study was to better understand the structure of naturally occurring opal-A using synchrotron X-ray total scattering coupled with PDF analysis, together with synchrotron XRD and TEM. Total scattering PDF analysis has been increasingly used to study local structures of amorphous, nano-crystalline and crystalline phases (Proffen et al. 2005; Billinge & Levin 2007; Gateshki et al. 2007; Billinge and Kanatzidis 2004; Lee and Xu 2020). In recent years, by taking advantage of high-flux high-resolution third-generation synchrotron X-ray sources combined with advanced detector technology and data processing algorithms, the PDF method has found numerous applications in characterizing the structures of complex materials such as disordered crystalline phases, nanomaterials, glasses, liquids and melts (e.g. Chupas et al. 2003; Juhás et al. 2013). Herein we have characterized the amorphous-like or poorly crystalline structure of opal-A (both opal-AN and opal-AG) using total X-ray scattering PDF analysis. Our analysis yields the atomic pair distances of opal-A, which are compared with those of amorphous silica gels, opal-CT, and silica polymorphs. In combination with synchrotron XRD and TEM, PDF analysis is a powerful approach for revealing the local structures (i.e., short- and medium-range orders) of opal-A as well as other poorly crystalline minerals (Xu et al. 2000, 2002; Zhang et al. 2002; Grangeon et al. 2015; Lee et al. 2019).

SAMPLES AND METHODS

The opal-AN (hyalite) sample is from Chalice mine, North Carolina, USA (Supplementary Fig. S1). It exhibits globular and botryoidal shapes of amorphous silica with glass-like appearance and a strong green fluorescence under UV light. The opal-AG sample is

from Spencer mine, Idaho, USA (Supplementary Fig. S2), and displays iridescent colors. For comparison, we also analyzed precious opal (opal-AG) from South Australia, opal-CT and synthetic silica gels. The opal-CT sample is part of a petrified wood slab from Arizona, USA. The amorphous silica gels were synthesized following a sol-gel procedure using tetraethyl orthosilicate (TEOS, $Si(OC_2H_5)_4$) at pH ~3 and pH ~9 (Zheng et al. 2019).

Laboratory XRD data were collected with a 2-D image-plate detector and a 0.3 mm collimator using a Rigaku Rapid II instrument (Mo-*K*α radiation) in the Department of Geoscience, University of Wisconsin-Madison. Two-dimensional diffraction images were converted to conventional 2θ vs. intensity plots using the Rigaku 2DP software. Electron probe microanalysis (EPMA) with wavelength-dispersive spectroscopy (WDS) was conducted using a CAMECA SXFiveFe electron microprobe at a voltage of 20 keV and a beam current of 15 nA in the Department of Geoscience, University of Wisconsin-Madison. TEM specimens were prepared by depositing a suspension of crushed grains on a lacy carbon-coated Cu grid. Bright-field and high-resolution TEM images with selected-area electron diffraction (SAED) patterns were obtained using a Philips CM200-UT transmission electron microscope operated at 200 keV in the Materials Science Center, University of Wisconsin-Madison. Chemical composition was determined using energy-dispersive spectroscopy (EDS) with a Li-drifted Si detector.

Synchrotron X-ray scattering experiments were conducted using X-rays with $\lambda = 0.24116$ Å at beamline 17-BM, Advanced Photon Source (APS), Argonne National Laboratory. Powders of opals and silica gels were placed inside polyimide tubes with an inner diameter of 1 mm. An amorphous Si area detector was used to collect 2D diffraction data in transmission geometry. Each single exposure on the area detector was set to 1 second, which was repeated 120 times for a total collection time of 120 seconds for each sample. The sample-to-detector distance and beam

center position were calibrated using a LaB_6 standard. Diffraction data of an empty polyimide tube were collected for background removal in data reduction. GSASII (Toby and Von Dreele 2013) was used to integrate and convert the 2-D patterns to 1-D intensity versus wave vector (Q) plots. The obtained data up to a Q_{max} of 19.9 $Å^{-1}$ were then transformed to PDF patterns using PdfGetX3 (Juhás et al. 2013). PDF fitting and refinement were carried out using the PDFGui software (Farrow et al. 2007). The fittings were performed between r_{min} = 1.2 Å and r_{max} = 10 Å. Starting structure models of cubic cristobalite, hexagonal tridymite and coesite (Levien and Prewitt 1981) were used to calculate PDF profiles and simulate XRD patterns. To test the multi-phase model of opal-A, several models incorporating interstratified cristobalite/tridymite layers, coesite nanodomains and the twinning/stacking faults between six-membered [SiO_4] rings were developed for the PDF refinement. Unit-cell parameters and scale factors were varied, while atomic coordinates and thermal factors were kept at the original values to minimize overparameterization.

RESULTS AND DISCUSSION

Bright-field TEM images and SAED patterns of opal-AN and opal-AG are shown in Figure 1. Opal-AN shows an aggregation of different sizes of nanograins (< 5nm) generating banded features (Figs. 1A-C). Locally, some areas in opal-AN exhibit almost an amorphous-like feature. Opal-AG contains silica nanospheres with a diameter of ~400 nm (Figs. 1D-E). It was reported that the spheres are primarily built from very fine nanograins (Gaillou et al. 2008b). SAED patterns of both opals show only one broad ring at ~4.0 Å (Figs. 1A and 1D). TEM EDS analysis indicates that they contain minor amounts of Na, Al, K, and Ca (Figs. 1G-H). This is consistent with the earlier study by Gaillou et al. (2008a), who reported that the main impurities in natural opals are Al, Ca, Fe, K, Na, and Mg. The mechanism of impurity incorporation in

opals is the substitution of Si^{4+} by Al^{3+} and the induced charge imbalance can be compensated by the addition of Ca^{2+}, Mg^{2+}, K^{+}, and Na^{+} (Gaillou et al. 2008a; Liesegang and Milke 2014). EPMA results of opal-AN and opal-AG show that their water content ranges from 6.52 – 9.92 wt.% and 6.14 – 7.25 wt.%, respectively (Supplementary Table. S1); H_2O contents were obtained by directly analyzing O using EPMA and then assigning the excessive O to H_2O. Natural opal can contain up to 20 wt.% water in the forms of silanol (R_3SiOH), trapped water, and absorbed water (Graetsch et al. 1990; Day and Jones 2008; Boboň et al. 2011). Jones and Renaut (2004) suggest that wet opal (12-13 wt.%) was formed as a result of rapid precipitation whereas the "dry" opal (5-6 wt.%) was formed due to slower precipitation.

Synchrotron XRD patterns of opal-CT, opal-AG, opal-AN and synthetic amorphous silica gels are shown in Figure 2. The synthetic amorphous gels, opal-AG and opal-AN have nearly identical XRD patterns except there are differences in the position of the first (main) diffraction peak. The *d*-spacings of the main peaks of silica gel-pH3, silica gel-pH9, opal-AN and opal-AG are 3.88(2) Å, 3.99(1) Å, 4.03(1) Å and 4.05(1) Å, respectively (Fig. 2). The main diffraction peak from ~3.9 to ~4.0 Å is manifested by increased disorder and diffuse scattering of the (111) reflection of cristobalite and the three main reflections of tridymite (Fig. 2). The most intense peak of opal-CT at 4.12 Å (Fig. 2) coincides with the combination of the (101) reflection of low-cristobalite and (002) reflection of low-tridymite (Jones and Segnit 1971). The increase of *d*-spacing of the main peak from silica gel (3.88 Å) to opal-AG (4.05 Å) to opal-CT (4.12 Å) suggets an increase in its structural order or more localized tridymitic/cristobalitc nanodomains (Fig. 2) (Graetsch and Ibel 1997).

Generally, opal-A is defined as having a broad ~4.0 Å diffraction peak only (Jones and Segnit 1971; Ghisoli et al. 2010). However, our high-intensity synchrotron XRD pattern with

low background facilitated the revelation of weaker extra peaks at ~2.00 Å, ~1.45 Å, and ~1.21 Å (Fig. 2). These extra peaks are also discernible in our Mo-*K*α radiation laboratory XRD (Supplementary Fig. S3) and previous X-ray scattering data (Graetsch et al. 1990). Thus, the XRD pattern of opal-A can be redefined as one prominent peak at ~4.0 Å with broad peaks at ~2.0 Å, ~1.45 Å, and ~1.21 Å. The diffraction peaks at 1.45 Å and 1.21 Å suggest a hexagonal (or pseudo-hexagonal) symmetry component, which is similar to the layered structures of clay minerals (i.e., *hk0* diffraction), 6-line ferrihydrite (Lee and Xu 2019b) and vernadite (Lee et al. 2019). The broad peak at ~2.0 Å is associated with the (004) reflection of orthorhombic tridymite and the (222) reflection of β-cristobalite (i.e., high cristobalite with a cubic symmetry). In addition, opal-AN and opal-AG exhibit a broad flat hump around ~2.44 Å (Fig. 2 & Supplementary Fig. S3). The distribution of diffuse intensity of opal-AN and opal-AG from ~7.0 Å to ~1.1 Å (i.e., 2º to 13º 2θ in Fig. 2) is similar to that of silica gels. By contrast, opal-CT shows much weaker diffuse intensity. XRD pattern of opal-CT shows three sharp diffraction peaks at 4.31, 4.12 and 2.51 Å, in addition to several weak and broad reflections (Fig. 2). The sharp peak of opal-CT at 2.51 Å is associated with the (310) and (020) reflections of orthorhombic tridymite and the (220) reflection of β-cristobalite. Previous HRTEM and SAED studies of opal-CT revealed that the needle-shaped opal-CT nanocrystals preferentially elongate along the [010] direction of the orthorhombic tridymite (Cady et al. 1996; Wilson 2014).

The PDF patterns of opal-A and opal-CT were calculated from the total X-ray scattering data (Fig. 3). For comparison, the PDF patterns of silica gel-pH3, silica gel-pH9, opal-AN, opal-AG and opal-CT are shown in supplementary Fig. S4. Opal-AN has two relatively stronger peaks at 1.61 Å and 2.64 Å than opal-AG (Supplementary Fig. S5). Otherwise, they show almost identical PDF profiles (Supplementary Fig. S5). We thus refer to both opal-AN and opal-AG as

205 "opal-A" in the following sections. Opal-A and silica-gels show short-range atomic pairs (below
206 ~15 Å and ~12 Å, respectively), while opal-CT contains medium-range atomic pairs (beyond 40
207 Å). Also, the PDF pattern of precious opal-AG from Idaho is almost the same as that of
208 Australian precious opal-AG (Supplementary Fig. S5). The first major peak at 1.61 Å
209 corresponds to Si–O correlations in [SiO_4] tetrahedra (Fig. 3). The second peak at 2.64 Å and the
210 third peak at 3.07 Å are due to O-O and Si-Si correlations in corner-sharing [SiO_4] tetrahedra
211 (Fig. 3). The peak damping is related to the size of ordered clusters (Farrow et al. 2007). Based
212 on the damping feature, the average size of ordered clusters of opal-A is slightly larger than that
213 in silica gels (Supplementary Fig. S4B).

214 The PDF pattern of opal-A is compared with those of other silica polymorphs from 1 to
215 10 Å (Fig. 3). Opal-A and opal-CT have very similar peak positions up to 10 Å, indicating that
216 they possess similar local structures. Figure 4 shows densities vs. the average Si-O bond
217 distances of several silica polymorphs. The Si-O bond of opal is longer than those of low-
218 tridymite and low-cristobalite (Fig. 4 & Supplementary Fig. S6). Hence, opal-A is a unique
219 mineraloid in the sense that its Si-O bond distance is similar to those of quartz and high-pressure
220 silica coesite, yet its density is much lower (Fig. 4).

221 Regarding explanation of the short Si-O distances (e.g., low-tridymite), Dollase (1967)
222 suggested the highly anisotropic thermal ellipsoids of oxygen atoms in [SiO_4]. Demuth et al.
223 (1999) proposed that the short distances are related to considerable strains in the structure, which
224 could be released by lowering the symmetry. The widely accepted structure model of opal
225 comprises the intergrowths of cristobalite and tridymite layered units of rigid corner-sharing
226 [SiO_4] tetrahedra (Jones et al. 1964; Sanders 1980; Curtis et al. 2019). The local [SiO_4]
227 tetrahedral arrangement of opals has been reported to be similar to those in other silica

polymorphs such as low-tridymite and low-cristobalite (Graetsch et al. 1990; Smith 1998). However, the PDF patterns of tridymite and cristobalite are not sufficient to explain the local structures of opal-A and opal-CT (especially the peak at 4.14 Å) (Fig. 3). Interestingly, the local structure of coesite can explain the peak at ~4.14 Å, suggesting the existence of the four-membered [SiO_4] tetrahedral units in both opal-A and opal-CT. As shown in Figure 3, the PDF profile of coesite shows similar peaks of opal-A and opal-CT up to 5.3 Å. The structure of coesite is analogous to that of feldspar and consists of rings of four [SiO_4] tetrahedra. On the other hand, the PDF profiles of quartz (with a helical structure) and melanophlogite (with 5-member rings) (Navrotsky et al. 2003; Xu et al. 2007) are significantly different from that of opal-A and opal-CT (Fig. 3). In the case of silica glass, previous studies reported that six-membered rings of [SiO_4] tetrahedra are the dominant structural unit with minor components of five- and four-membered rings (Meade et al. 1992; Inamura et al. 1997; Pasquarello and Car 1998; Sato and Funamori 2008). The concentrations of five- and four-membered rings vary with the water content and precipitation condition of silica glass (Pasquarello and Car 1998; Urakawa et al. 2020). Urakawa et al. (2020) reported that hydrous silica glass contains a larger population of smaller rings than dry glass due to the breaking SiO_4 linkages with the OH group. Therefore, the water in opal can contribute to the formation of a significant amount of four-member [SiO_4] tetrahedral rings (i.e. coesite unit) in the structure. Lee et al. (2020) reported that impact-induced phase transformation of opal-A to coesite at pressures (~0.6 – 0.7 GPa), significantly lower than the transition pressure of quartz to coesite (~2 GPa). They suggested that the lower phase transformation pressure of opal-A is associated with its local precursor structure (the four-membered rings or coesite clusters) and water content (Lee et al. 2020).

Both tridymite and cristobalite consist of six-membered rings of [SiO_4] tetrahedra, but they differ in the stacking sequences (Sanders 1980). For opal-CT, previous studies used the interstratified layers of cristobalite and tridymite for structural modeling (Guthire et al. 1995; Wilson 2014). Our experimental PDF pattern of opal-A (Fig. 3) indicates that its structure is mainly a mixture of six- and four-membered [SiO_4] rings, while five-membered rings (melanophlogite-like structure) are not evident. We carried out structure refinement of opal-A by fitting the experimental PDF profile using an interstratified structure of tridymite and cristobalite (in a 4:3 ratio) and coesite nanodomain / cluster (5.3 Å crystallite size) (Fig. 6A).

The four-membered rings could be dominant on the surface of tridymite/cristobalite nanodomains in opal-A, which may block the growth of these nanodomains (Fig. 5E). Moreover, the four-membered rings can be generated by twinning and stacking faults of six-membered rings, which also produce eight-membered rings together with 4-membered rings (Fig. 5D). To account for the planar defect in opal structure, we propose a superstructure model of four-, six- and eight-membered rings followed by twinning (Supplementary Fig. S7 & Supplementary Text). PDF structure refinement was carried out using this interstratified structure, coesite nanodomain, and the twin boundary model (Fig. 6B). Importantly, addition of the four- and eight-membered ring structure resolved the mismatch around ~7.6 Å, which, though, is mainly related to the structure of eight-membered rings (Fig. 6B). The refined scale factors are 1.08, 0.22, and 0.10, for the interstratified phase, coesite nanodomain and the twin boundary, respectively (Fig. 6B). The interstratified phase can account for stacking disorder or interstratification between cristobalite and tridymite in the 4:3 ratio, and the final refined scale factors of cristobalite, tridymite, coesite, and the twin boundary are 0.62, 0.46, 0.22, and 0.10, respectively.

Figure 3 shows that the structure of opal-A is similar to those of low-tridymite and low-cristobalite. A simple mixture model of tridymite and cristobalite was also tested in PDF fitting of opal-A (Fig. 6C). The PDF refinement used low-tridymite, low-cristobalite, coesite nanodomain, and twin boundary model, suggesting the occurrence of clusters of 6-membered rings of cristobalite and tridymite, 4-membered rings and 8-membered rings in the opal-A structure (Fig. 6C). The scale factors are 0.69, 0.46, 0.21, and 0.11, respectively. Combining all the components, PDF refinement of opal-A was carried out using five structure components of the interstratified structure, cristobalite, tridymite, coesite nanodomain, and the twin boundary (Fig. 6D). The scale factors are 0.54, 0.34, 0.23, 0.21, and 0.09, respectively. It assigns the interstratified phase (to model stacking disorder or interstratification between cristobalite and tridymite) to cristobalite (0.31) and tridymite (0.23) portions, and the scale factors for cristobalite, tridymite, coesite, and the twin boundary are 0.65, 0.46, 0.21, 0.09, respectively. The normalized percentages of cristobalite, tridymite, coesite, and the twin boundary for the four cases are listed in supplementary Table. S2. The scale factors indicate mass fractions of each phase. The scale factors for case 6D is between those of case B and case C (Figure 6). The results of PDF analysis suggest that opal-A contains more cristobalite components than tridymite components (Fig. 6). Based on the differences between experimental and calculated PDF patterns, the natural opal-A structure shows an acceptable agreement with the proposed model. Remaining residuals at the 1.61 Å, 2.64 Å, 3.07 Å, and 4.07 Å peaks (Fig. 6) may be caused by local distortions of the silica tetrahedral rings connecting the neighboring domains. Similarly, several studies reported the atomic structures of amorphous phases and nanomaterials by fitting multiple models to a pair distribution function (Proffen et al. 2005; Gateshki et al. 2007; Lee et al. 2019).

296 Finally, the powder XRD pattern was simulated using a mixture model of cristobalite,
297 tridymite, and coesite to verify our proposed opal-A structure (Fig. 7). Based on the scale factors
298 of PDF refinement, the proportions of these three phases are estimated. Overall, the simulated
299 XRD pattern is well matched with the experimental XRD pattern of opal-A. The right shoulder
300 of the asymmetrical diffraction peak at 4.03 Å can be explained by the occurrence of the coesite
301 component. Overall, the XRD and PDF results support the occurrence of coesite-like clusters
302 (i.e. four-membered [SiO_4] rings) in the opal-A structure. The framework of four-membered
303 rings is similar to that of feldspar structure (Megaw 1970). TEM-EDS (Figs. 2G and 2H) shows
304 that the opal-A contains minor K, Na, Al, and Ca impurities that could be incorporated into the
305 clusters or domains with four-membered [SiO_4] rings. Furthermore, the average density of
306 silanol hydroxyl (Si-OH) groups of coesite, tridymite, and cristobalite are 0.059 $Å^{-2}$, 0.058 $Å^{-2}$,
307 and 0.055A $Å^{-2}$, respectively (unlike quartz's much higher silanol hydroxyl densities, 0.070 $Å^{-2}$)
308 (Murashov and Demchuk 2005). Hence, the three phases have similar surface sites and unrelaxed
309 surface energies of tetrahedral silica, promoting the mixing of these components in the opal-A
310 structure.
311
312 **IMPLICATIONS**
313 Both synchrotron XRD and Mo-*K*α radiation laboratory XRD clearly reveal a number of
314 extra broad peaks in opal-A in addition to its main diffraction peak at ~4.0 Å. Previous studies
315 only used the ~4.0 Å peak for the definition of opal-A (Jones et al. 1964; Sanders 1980; Curtis et
316 al. 2019). Thus, the diffraction pattern of opal-A can be redefined as one prominent peak at ~4.0
317 Å plus three broad peaks at ~2.0 Å, ~1.45 Å and ~1.2 Å. The diffraction peaks of opal-A can be
318 explained by intergrowths of cristobalite and tridymite. The diffraction peaks at 1.45 Å and 1.2 Å

suggest a hexagonal (or pseudo-hexagonal) symmetry component in the opal structure. Our PDF analyses additionally reveal the occurrence of four- and eight-membered silica rings in the opal-A structure, via twinning, stacking faults, and interface boundaries of six-membered rings. Trace elements such as K, Na, Al and Ca can be incorporated into the coesite-like local structure, which is similar to the feldspar framework, in opal. In short, opal-A is mainly a mixture of ordered clusters of six- and four-membered rings, as manifested by interstratification of cristobalite and tridymite layers, inter-grown with coesite nanodomains. Similar locally ordered structures occur in other poorly crystallized nano-minerals such as vernadite (Lee and Xu 2020a). The multi-phase model of vernadite shows a mixture of ~7 Å phase, ~10 Å phase and their interstratified phases of manganese oxide layers (Lee et al. 2019; Lee and Xu 2020). It is expected that more poorly crystallized nano-minerals will be founded in nature as mixtures of multiple phases at short- and medium-range scales. Further studies on other opal structures (e.g., opal-CT and opal-C) using the combined XRD/PDF method are needed to better understand the natural opal structure. For example, in sedimentary cherts such as Monterey formation, the sediment silica undergoes a continuous transformation from opal-A (diatomaceous clay) through opal-CT to chert during the diagenesis (Kastner et al. 1977; Behl et al. 1994). This combined approach will provide detailed structural information of the phase transformation of opal with implications to its stability in geological environments.

ACKNOWLEDGMENTS

We thank Dr. Alejandro Fernandez-Martinez and an anonymous reviewer for constructive comments and Associate Editor Adam Wallace for editorial handling. We acknowledge the supports from National Science Foundation (EAR-1530614) and NASA Astrobiology Institute (NNA13AA94A), and Department of Geoscience of the University of

Wisconsin-Madison. Synchrotron X-ray experiments were performed at beamline 17-BM, Advanced Photon Source (APS), Argonne National Laboratory. APS is a U.S. Department of Energy (DOE) Office of Science User Facility operated for the DOE Office of Science by Argonne National Laboratory under Contract No. DE-AC02-06CH11357. We are grateful to Dr. Wenqian Xu for his help during the synchrotron experiments. This work was also supported by the Laboratory Directed Research and Development (LDRD) program at Los Alamos National Laboratory (LANL). LANL, an affirmative action/equal opportunity employer, is managed by Triad National Security Administration of the U.S. Department of Energy under contract number 89233218CNA000001.

REFERENCES

Antao, S.M., Hassan, I., Wang, J., Lee, P.L., and Toby, B.H. (2008) State-of-the-art high-resolution powder X-ray diffraction (HRPXRD) illustrated with Rietveld structure refinement of quartz, sodalite, tremolite, and meionite. The Canadian Mineralogist, 46(6), 1501-1509.

Araki, T., and Zoltai, T. (1969) Refinement of a coesite structure. Zeitshrift fur Kristallographie 120, 381-387.

Behl, R. J., Garrison, R. E., Iijima, I., Abed, A., and Garrison, R. (1994) The origin of chert in the Monterey Formation of California (USA). In Siliceous, phosphatic and glauconitic sediments of the Tertiary and Mesozoic: Proceedings of the 29th International Geological Congress, Part C, 101-132.

Billinge, S.J., and Kanatzidis, M.G. (2004) Beyond crystallography: the study of disorder, nanocrystallinity and crystallographically challenged materials with pair distribution functions. Chemical communications(7), 749-760.

Boboň, M., Christy, A.A., Kluvanec, D., and Illášová, L. (2011) State of water molecules and silanol groups in opal minerals: a near infrared spectroscopic study of opals from Slovakia. Physics and Chemistry of Minerals, 38(10), 809-818.

Billinge, S.J., and Kanatzidis, M.G. (2004) Beyond crystallography: the study of disorder, nanocrystallinity and crystallographically challenged materials with pair distribution functions. Chemical communications(7), 749-760.

Billinge, S. J., & Levin, I. (2007). The problem with determining atomic structure at the nanoscale. science, 316(5824), 561-565.

Boboň, M., Christy, A.A., Kluvanec, D., and Illášová, L. (2011) State of water molecules and silanol groups in opal minerals: a near infrared spectroscopic study of opals from Slovakia. Physics and Chemistry of Minerals, 38(10), 809-818.

Brown, L., Ray, A., and Thomas, P. (2003) ^{29}Si and ^{27}Al NMR study of amorphous and paracrystalline opals from Australia. Journal of Non-Crystalline Solids, 332(1-3), 242-248.

Cady, S. L., Wenk, H. R., and Downing, K. H. (1996) HRTEM of microcrystalline opal in chert and porcelanite from the Monterey Formation, California. American Mineralogist, 81(11-12), 1380-1395.

384 Chester, R., and Elderfield, H. (1968) The infrared determination of opal in siliceous deep-sea
385 sediments. Geochimica et Cosmochimica Acta, 32(10), 1128-1140.
386 Chupas, P.J., Qiu, X., Hanson, J.C., Lee, P.L., Grey, C.P., and Billinge, S.J. (2003) Rapid-
387 acquisition pair distribution function (RA-PDF) analysis. Journal of Applied
388 Crystallography, 36(6), 1342-1347.
389 Clarke, J. (2003) The occurrence and significance of biogenic opal in the regolith. Earth-Science
390 Reviews, 60(3-4), 175-194.
391 Curtis, N.J., Gascooke, J.R., Johnson, M.R., and Pring, A. (2019) A Review of the Classification
392 of Opal with Reference to Recent New Localities. Minerals, 9(5), 299.
393 Darragh, P., Gaskin, A., and Sanders, J. (1976) Opals. Scientific American, 234(4), 84-95.
394 Day, R., and Jones, B. (2008) Variations in water content in opal-A and opal-CT from geyser
395 discharge aprons. Journal of Sedimentary Research, 78(4), 301-315.
396 Demuth, T., Jeanvoine, Y., Hafner, J., and Angyan, J. G. (1999) Polymorphism in silica studied
397 in the local density and generalized-gradient approximations. Journal of Physics:
398 Condensed Matter, 11(19), 3833.
399 Dollase, W., and Baur W.H. (1976) The superstructure of meteoritic low tridymite solved by
400 computer simulation. American Mineralogist, 61, 971-978.
401 Eckert, A. W. (1997). The world of opals, 9-20 p. Wiley, New York.
402 Elzea, J., Odom, I., and Miles, W. (1994) Distinguishing well ordered opal-CT and opal-C from
403 high temperature cristobalite by X-ray diffraction. Analytica Chimica Acta, 286(1), 107-
404 116.
405 Farrow, C., Juhas, P., Liu, J., Bryndin, D., Božin, E., Bloch, J., Proffen, T., and Billinge, S.
406 (2007) PDFfit2 and PDFgui: computer programs for studying nanostructure in crystals.
407 Journal of Physics: Condensed Matter, 19(33), 335219.
408 Gaillou, E., Delaunay, A., Rondeau, B., Bouhnik-le-Coz, M., Fritsch, E., Cornen, G., and
409 Monnier, C. (2008a) The geochemistry of gem opals as evidence of their origin. Ore
410 Geology Reviews, 34(1-2), 113-126.
411 Gaillou, E., Fritsch, E., Aguilar-Reyes, B., Rondeau, B., Post, J., Barreau, A., and Ostroumov,
412 M. (2008b) Common gem opal: An investigation of micro-to nano-structure. American
413 Mineralogist, 93(11-12), 1865-1873.

Gateshki, M., Niederberger, M., Deshpande, A. S., Ren, Y., & Petkov, V. (2007). Atomic-scale structure of nanocrystalline CeO_2–ZrO_2 oxides by total X-ray diffraction and pair distribution function analysis. Journal of Physics: Condensed Matter, 19(15), 156205.

Ghisoli, C., Caucia, F., and Marinoni, L. (2010) XRPD patterns of opals: A brief review and new results from recent studies. Powder Diffraction, 25(3), 274-282.

Gies, H. (1983) Studies on clathrasils. III. Crystal structure of melanophlogite, a natural clathrate compound of silica. Zeitshrift fur Kristallographie, 164, 247-57.

Graetsch, H., and Ibel, K. (1997) Small angle neutron scattering by opals. Physics and Chemistry of Minerals, 24(2), 102-108.

Graetsch, H., Mosset, A., and Gies, H. (1990) XRD and ^{29}Si MAS-NMR study on some non-crystalline silica minerals. Journal of Non-Crystalline Solids, 119(2), 173-180.

Grangeon, S., Fernandez-Martinez, A., Warmont, F., Gloter, A., Marty, N., Poulain, A., and Lanson, B. (2015) Cryptomelane formation from nanocrystalline vernadite precursor: a high energy X-ray scattering and transmission electron microscopy perspective on reaction mechanisms. Geochemical transactions, 16(1), 1-16.

Guthrie, G. D., Dish, D. L., and Reynolds, R. C. (1995) Modeling the X-ray diffraction pattern of opal-CT. American Mineralogist, 80(7-8), 869-872.

Hatipog, M., Can, N., and Karali, T. (2010) Effects of heating on fire opal and diaspore from Turkey. Physica B: Condensed Matter, 405(7), 1729-1736.

Hirose, T., Kihara, K., Okuno, M., Fujinami, S., and Shinoda, K. (2005) X-ray, DTA and Raman studies of monoclinic tridymite and its higher temperature orthorhombic modification with varying temperature. Journal of Mineralogical and Petrological Sciences, 100(2), 55-69.

Ilieva, A., Mihailova, B., Tsintsov, Z., and Petrov, O. (2007) Structural state of microcrystalline opals: A Raman spectroscopic study. American Mineralogist, 92(8-9), 1325-1333.

Inamura, Y., Arai, M., Kitamura, N., Bennington, S., and Hannon, A. (1997) Intermediate-range structure and low-energy dynamics of densified SiO2 glass. Physica B: Condensed Matter, 241, 903-905.

Jones, J., Sanders, J., and Segnit, E. (1964) Structure of opal. Nature, 204(4962), 990-991.

Jones, J., and Segnit, E. (1971) The nature of opal I. Nomenclature and constituent phases. Journal of the Geological Society of Australia, 18(1), 57-68.

Jones, B., and Renaut, R.W. (2004) Water content of opal-A: implications for the origin of laminae in geyserite and sinter. Journal of Sedimentary Research, 74(1), 117-128.

Juhás, P., Davis, T., Farrow, C.L., and Billinge, S.J. (2013) PDFgetX3: a rapid and highly automatable program for processing powder diffraction data into total scattering pair distribution functions. Journal of Applied Crystallography, 46(2), 560-566.

Kastner, M., Keene, J. B., and Gieskes, J. M. (1977) Diagenesis of siliceous oozes—I. Chemical controls on the rate of opal-A to opal-CT transformation—an experimental study. Geochimica et Cosmochimica Acta, 41(8), 1041-1059.

Lee, M., MacLaren, I., Andersson, S., Kovacs, A., Tomkinson, T., Mark, D., and Smith, C. (2015) Opal-A in the Nakhla meteorite: A tracer of ephemeral liquid water in the Amazonian crust of Mars. Meteoritics & planetary science, 50(8), 1362-1377.

Lee, S., and Xu, H. (2019a) Using powder XRD and pair distribution function to determine anisotropic atomic displacement parameters of orthorhombic tridymite and tetragonal cristobalite. Acta Crystallographica Section B: Structural Science, Crystal Engineering and Materials, 75(2).

Lee, S., and Xu, H. (2019b). One-Step Route Synthesis of Siliceous Six-Line Ferrihydrite: Implication for the Formation of Natural Ferrihydrite. ACS Earth and Space Chemistry, 3(4), 503-509.

-. (2020) Using Complementary Methods of Synchrotron Radiation Powder Diffraction and Pair Distribution Function to Refine Crystal Structures with High Quality Parameters—A Review. Minerals, 10(2), 124.

Lee, S., Xu, H., Xu, W., and Sun, X. (2019) The structure and crystal chemistry of vernadite in ferromanganese crusts. Acta Crystallographica Section B: Structural Science, Crystal Engineering and Materials, 75(4).

Lee, S., Cai, J., Jin, S., Zhang, D., Thevamaran, R., and Xu, H. (2020). Coesite Formation at Low Pressure during Supersonic Microprojectile Impact of Opal. ACS Earth and Space Chemistry, 4(8), 1291-1297.

Levien, L., and Prewitt, C.T. (1981) High-pressure crystal structure and compressibility of coesite. American Mineralogist, 66(3-4), 324-333.

Levien, L., Prewitt, C.T., and Weidner, D.J. (1980) Structure and elastic properties of quartz at pressure. American Mineralogist, 65(9-10), 920-930.

476 Liesegang, M., and Milke, R. (2014) Australian sedimentary opal-A and its associated minerals:
477 Implications for natural silica sphere formation. American Mineralogist, 99(7), 1488-
478 1499.
479 Meade, C., Hemley, R.J., and Mao, H. (1992) High-pressure X-ray diffraction of SiO_2 glass.
480 Physical Review Letters, 69(9), 1387.
481 Megaw, H.D. (1970) Structural relationship between coesite and feldspar. Acta
482 Crystallographica Section B: Structural Crystallography and Crystal Chemistry, 26(3),
483 261-265.
484 Meral, C. (2012) The study of disorder in amorphous silica, alkali-silica reaction gel and fly ash.
485 UC Berkeley.
486 Mortlock, R.A., and Froelich, P.N. (1989) A simple method for the rapid determination of
487 biogenic opal in pelagic marine sediments. Deep Sea Research Part A. Oceanographic
488 Research Papers, 36(9), 1415-1426.
489 Murashov, V.V., and Demchuk, E. (2005) Surface sites and unrelaxed surface energies of
490 tetrahedral silica polymorphs and silicate. Surface science, 595(1-3), 6-19.
491 Murray, R.W., Leinen, M., and Knowlton, C.W. (2012) Links between iron input and opal
492 deposition in the Pleistocene equatorial Pacific Ocean. Nature Geoscience, 5(4), 270-274.
493 Navrotsky, A., Xu, H., Moloy, E.C., and Welch, M.D. (2003) Thermochemistry of guest-free
494 melanophlogite. American Mineralogist, 88 (10), 1612-1614.
495 Paris, M., Fritsch, E., and Reyes, B.O.A. (2007) ^{1}H, ^{29}Si and ^{27}Al NMR study of the
496 destabilization process of a paracrystalline opal from Mexico. Journal of Non-Crystalline
497 Solids, 353(16-17), 1650-1656.
498 Pasquarello, A., and Car, R. (1998) Identification of Raman defect lines as signatures of ring
499 structures in vitreous silica. Physical Review Letters, 80(23), 5145.
500 Pewkliang, B., Pring, A., and Brugger, J. (2008) The formation of precious opal: clues from the
501 opalization of bone. The Canadian Mineralogist, 46(1), 139-149.
502 Proffen, T., Page, K. L., McLain, S. E., Clausen, B., Darling, T. W., TenCate, J. A., ... &
503 Ustundag, E. (2005). Atomic pair distribution function analysis of materials containing
504 crystalline and amorphous phases. Zeitschrift für Kristallographie-Crystalline Materials,
505 220(12), 1002-1008.

Ragueneau, O., Tréguer, P., Leynaert, A., Anderson, R., Brzezinski, M., DeMaster, D., Dugdale, R., Dymond, J., Fischer, G., and Francois, R. (2000) A review of the Si cycle in the modern ocean: recent progress and missing gaps in the application of biogenic opal as a paleoproductivity proxy. Global and Planetary Change, 26(4), 317-365.

Raman, C., and Jayaraman, A. (1953) The structure of opal and the origin of its iridescence. Proceedings of the Indian Academy of Sciences-Section A, 38, p. 101-108. Springer.

Rapin, W., Chauviré, B., Gabriel, T., McAdam, A., Ehlmann, B.L., Hardgrove, C., Meslin, P.Y., Rondeau, B., Dehouck, E., and Franz, H. (2018) In situ analysis of opal in Gale Crater, Mars. Journal of Geophysical Research: Planets, 123(8), 1955-1972.

Rice, S., Freund, H., Huang, W., Clouse, J., and Isaacs, C. (1995) Application of Fourier transform infrared spectroscopy to silica diagenesis; the opal-A to opal-CT transformation. Journal of Sedimentary Research, 65(4a), 639-647.

Sanders, J. (1964) Colour of precious opal. Nature, 204(4964), 1151-1153.

-. (1980) Close-packed structures of spheres of two different sizes I. Observations on natural opal. Philosophical Magazine A, 42(6), 705-720.

Sato, T., and Funamori, N. (2008) Sixfold-coordinated amorphous polymorph of SiO_2 under high pressure. Physical review letters, 101(25), 255502.

Smith, D.K. (1998) Opal, cristobalite, and tridymite: noncrystallinity versus crystallinity, nomenclature of the silica minerals and bibliography. Powder diffraction, 13(1), 2-19.

Sun, V.Z., and Milliken, R.E. (2018) Distinct geologic settings of opal-A and more crystalline hydrated silica on Mars. Geophysical Research Letters, 45(19), 10,221-10,228.

Toby, B.H., and Von Dreele, R.B. (2013) GSAS-II: the genesis of a modern open-source all purpose crystallography software package. Journal of Applied Crystallography, 46(2), 544-549.

Tribaudino, M., Artoni, A., Mavris, C., Bersani, D., Lottici, P.P., and Belletti, D. (2008) Single-crystal X-ray and Raman investigation on melanophlogite from Varano Marchesi (Parma, Italy). American Mineralogist, 93(1), 88-94.

Urakawa, S., Inoue, T., Hattori, T., Sano-Furukawa, A., Kohara, S., Wakabayashi, D., Sato, T., Funamori, N., and Funakoshi, K.I. (2020) X-ray and neutron study on the structure of hydrous SiO_2 glass up to 10 GPa. Minerals, 10(1), 84.

536 Wilson, M. (2014) The structure of opal-CT revisited. Journal of non-crystalline solids, 405, 68-
537 75.
538 Xu, H., Heaney, P.J., and Beall, G.H. (2000) Phase transitions induced by solid solution in
539 stuffed derivatives of quartz: A powder synchrotron XRD study of the $LiAlSiO_4$-SiO_2
540 join. American Mineralogist, 85(7-8), 971-979.
541 Xu, H., Navrotsky, A., Balmer, M.L., and Su, Y. (2002) Crystal chemistry and phase transitions
542 in substituted pollucites along the $CsAlSi_2O_6$-$CsTiSi_2O_{6.5}$ Join: A powder synchrotron X-
543 ray diffractometry study. Journal of the American Ceramic Society, 85 (5), 1235-1242.
544 Xu, H., Zhang, J., Zhao, Y., Guthrie, G. D., Hickmott, D. D., and Navrotsky, A. (2007)
545 Compressibility and pressure-induced amorphization of guest-free melanophlogite: An
546 in-situ synchrotron X-ray diffraction study. American Mineralogist, 92(1), 166-173.
547 Zhang, J., Celestian, A., Parise, J.B., Xu, H., and Heaney, P.J. (2002) A new polymorph of
548 eucryptite ($LiAlSiO_4$), ε-eucryptite, and thermal expansion of α- and ε-eucryptite at high
549 pressure. American Mineralogist, 87 (4), 566-571.
550 Zheng, X.Y., Beard, B.L., and Johnson, C.M. (2019) Constraining silicon isotope exchange
551 kinetics and fractionation between aqueous and amorphous Si at room temperature.
552 Geochimica et Cosmochimica Acta, 253, 267-289.
553

554 **Figure captions**

555

556 **Figure 1.** Bright-field TEM images and SAED patterns of opal-AN (A-C) and opal-AG (D-F).
557 TEM X-ray EDS spectra of (G) opal-AN and (H) opal-AG showing the presence of Na, Al, Ca,
558 and K impurities. The C peak is from the lacey carbon-coated TEM grid.

559

560 **Figure 2.** Synchrotron XRD patterns of opal-CT, opal-AG, opal-AN, and synthetic amorphous
561 SiO_2 (pH3 and pH9) with reference peaks of cristobalite indexed by cubic symmetry (Lee and
562 Xu 2019a), orthorhombic tridymite (Lee and Xu 2019a) and coesite (Levien and Prewitt 1981).
563 Calculated diffraction patterns are listed for comparison. The d-values were calculated based on
564 the most intense diffraction maxima.

565

566 **Figure 3.** PDF pattern of opal-A from 1 to 10 Å range inserted with a structure model of two
567 corner-shared silica tetrahedra, compared with those of opal-CT, low-tridymite (Lee and Xu
568 2019a), low-cristobalite (Lee and Xu 2019a), coesite (Levien and Prewitt 1981), low-quartz
569 (Levien et al. 1980), and melanophlogite (Nakagawa et al. 2001).

570

571 **Figure 4.** Densities versus average Si-O bond distances of silica polymorphs. Orthorhombic
572 tridymite (Lee and Xu 2019a), orthorhombic tridymite (Dollase and Baur 1976), melanophlogite
573 (Tribaudino et al. 2008), melanophlogite (Gies 1983), monoclinic tridymite (Hirose et al. 2005),
574 monoclinic tridymite (Dollase and Baur 1976), cristobalite (Lee and Xu 2019a), low-quartz
575 (Antao et al. 2008), low-quartz[9] (Levien et al. 1980), coesite (Levien and Prewitt 1981), and
576 coesite (Araki and Zoltai 1969), opals (Eckert 1997), and the calculated anhydrous opal using the
577 PDF refinement result of this study.

578

579 **Figure 5.** Schematic structure models of opal-A including (A) six-membered rings of [SiO_4]
580 tetrahedra (tridymite- and cristobalite-like) along two different directions, (B) four-membered
581 rings (coesite-like), (C) Interstratified model of cristobalite and tridymite layers, (D) twinning of
582 six-membered rings, (E) surface structure of opal showing four-membered rings to block the
583 growth of six-membered rings, and (F) stacking faults between six-membered rings.

584

585 **Figure 6.** (A) PDF refinement of opal-A from 1.2 to 10 Å using models of the interstratified
586 structure of cristobalite and tridymite layers (in a 4:3 ratio) and coesite nanodomains (5.4 nm
587 crystallite size). The scale factors of the interstratification and coesite are 1.22 and 0.26,
588 respectively. (B) PDF refinement using the interstratification, coesite nanodomain, and the twin
589 boundary model (supplementary Fig. S7). The scale factors are 1.08 (0.62 for cristobalite, 0.46
590 for tridymite), 0.22, and 0.10, respectively. (C) PDF refinement using low-cristobalite (Lee and
591 Xu 2019a), low-tridymite (Lee and Xu 2019a), coesite nanodomain, and the twin boundary
592 model. The scale factors are 0.69, 0.46, 0.21, and 0.11, respectively. (D) PDF refinement using
593 interstratified structure, low-cristobalite, low-tridymite, coesite nanodomain, and the twin
594 boundary model. The scale factors are 0.54 (0.31 for cristobalite, 0.23 for tridymite), 0.34, 0.23,
595 0.21, and 0.09, respectively. The scale factors represent the unit cell fractions (mass fractions) of
596 all the phases. Black curve: experimental data; red curve: calculated profile; gray curve:
597 differences between the experimental and calculated PDF patterns. The normalized percentages
598 of cristobalite, tridymite, coesite, and the twin boundary are listed in Supplementary Table. S2.
599
600 **Figure 7.** XRD simulation of opal-A using a mixture of cristobalite (50%), monoclinic tridymite
601 (35%), and coesite (15%) with crystallite sizes of 1 nm, 1 nm and 0.5 nm, respectively,
602 calculated by CrystalMaker 9.2 software. The simulated XRD pattern does not take into account
603 the effects of the cluster or domain shapes.

This is the peer-reviewed, final accepted version for American Mineralogist, published by the Mineralogical Society of America.
The published version is subject to change. Cite as Authors (Year) Title. American Mineralogist, in press.
DOI: https://doi.org/10.2138/am-2022-8017. http://www.minsocam.org/

Fig.1

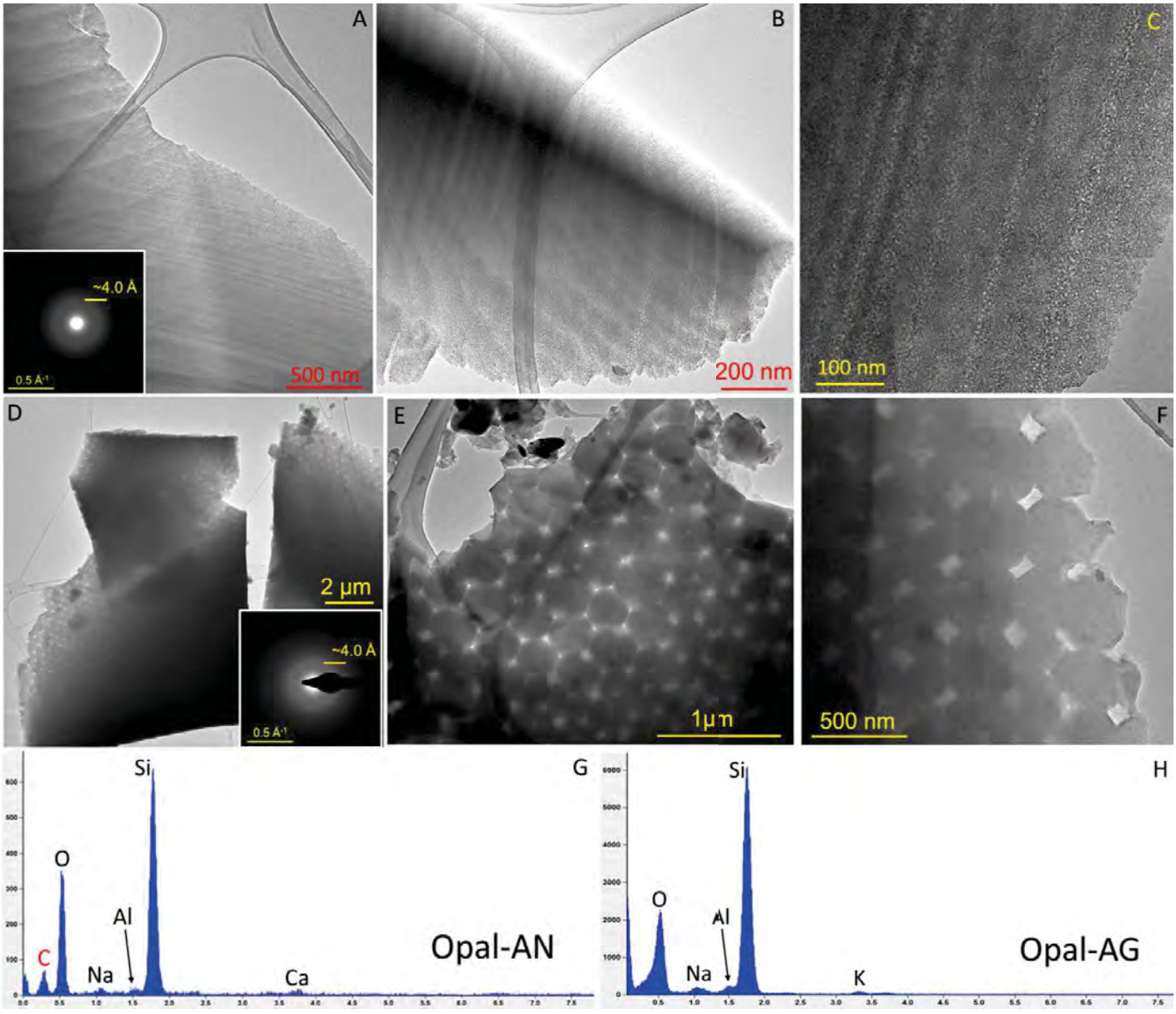

This is the peer-reviewed, final accepted version for American Mineralogist, published by the Mineralogical Society of America.
The published version is subject to change. Cite as Authors (Year) Title. American Mineralogist, in press.
DOI: https://doi.org/10.2138/am-2022-8017. http://www.minsocam.org/

Fig.2

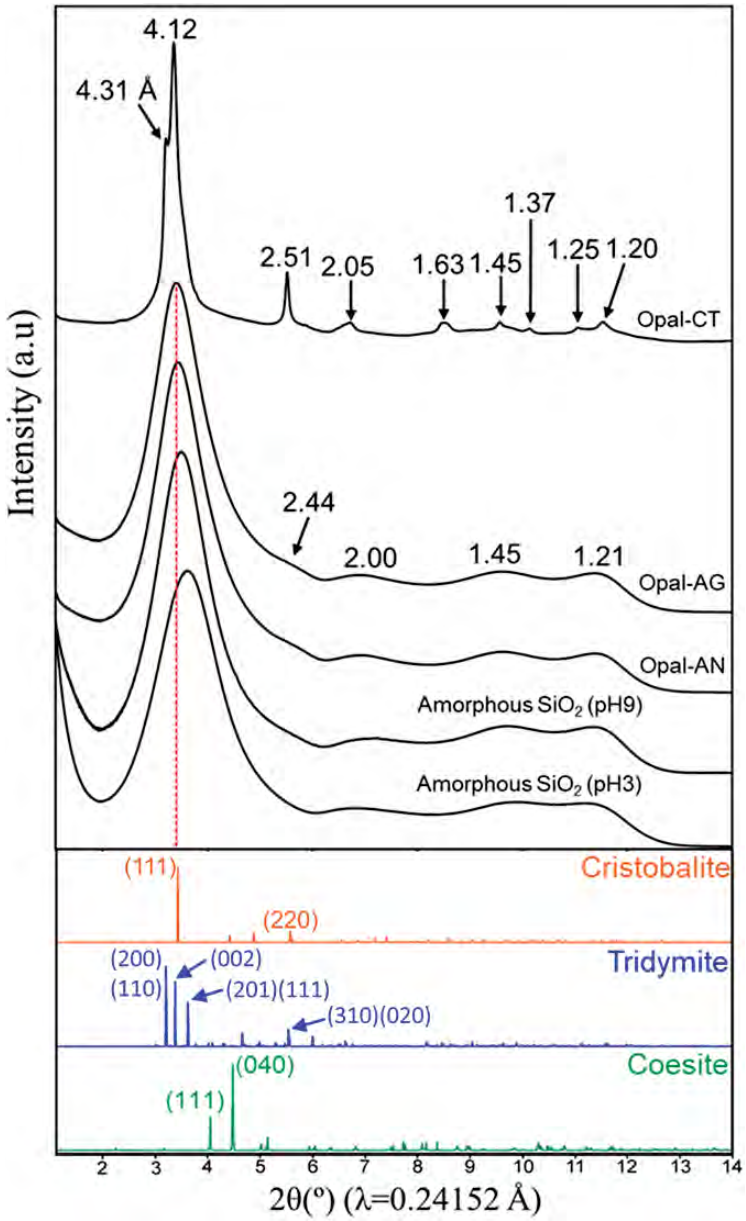

This is the peer-reviewed, final accepted version for American Mineralogist, published by the Mineralogical Society of America.
The published version is subject to change. Cite as Authors (Year) Title. American Mineralogist, in press.
DOI: https://doi.org/10.2138/am-2022-8017. http://www.minsocam.org/

Fig.3

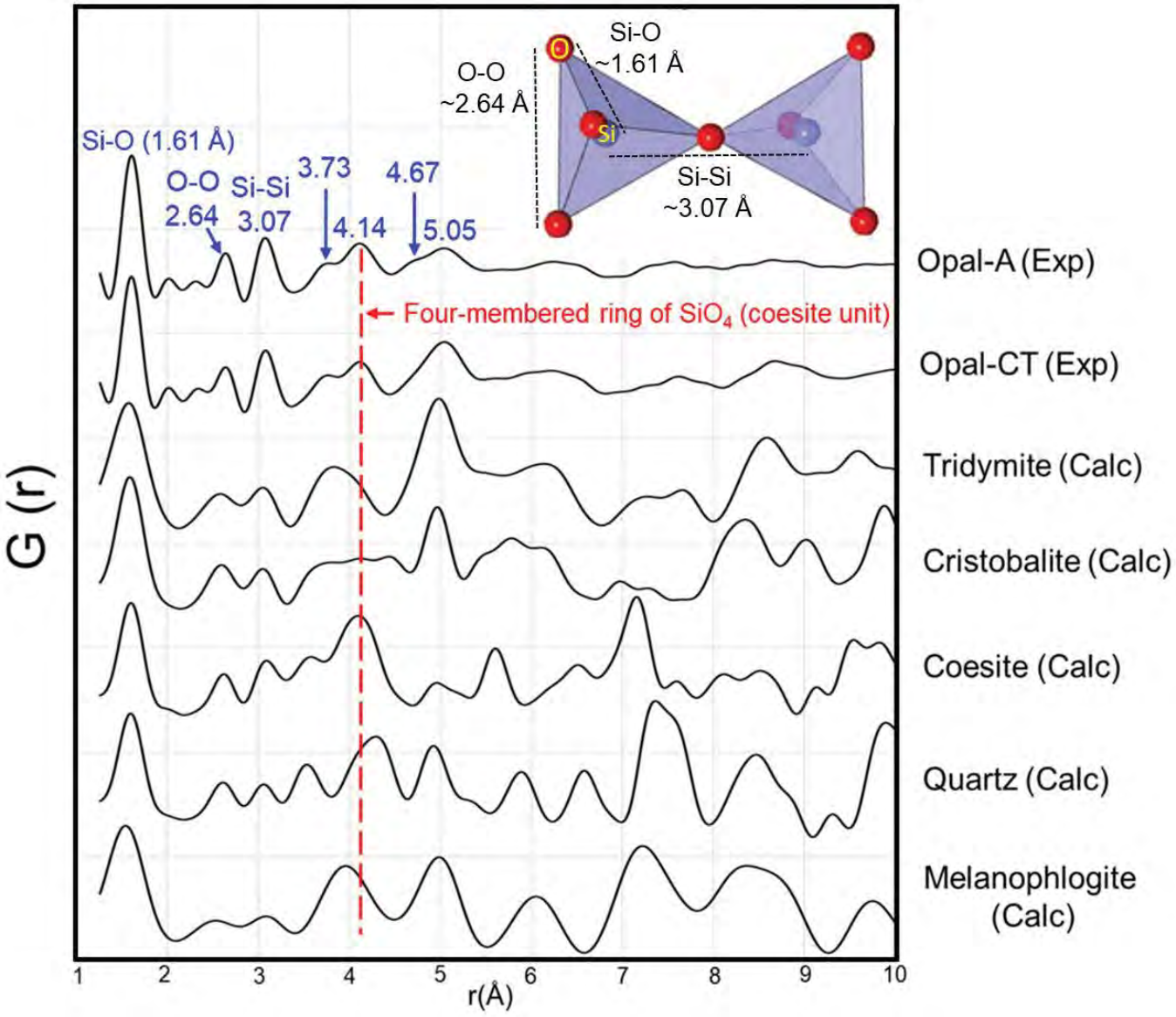

This is the peer-reviewed, final accepted version for American Mineralogist, published by the Mineralogical Society of America.
The published version is subject to change. Cite as Authors (Year) Title. American Mineralogist, in press.
DOI: https://doi.org/10.2138/am-2022-8017. http://www.minsocam.org/

Fig.4

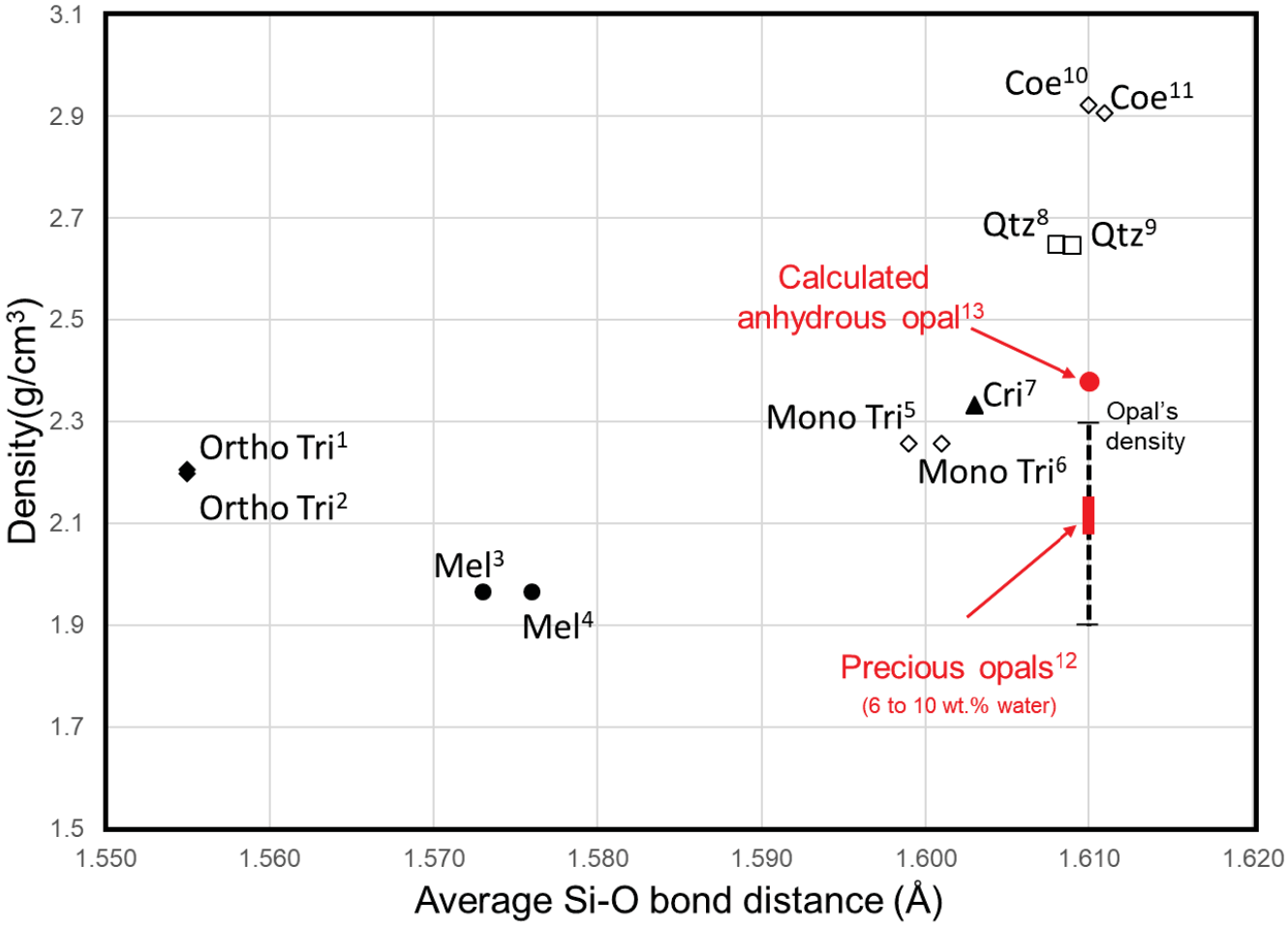

This is the peer-reviewed, final accepted version for American Mineralogist, published by the Mineralogical Society of America.
The published version is subject to change. Cite as Authors (Year) Title. American Mineralogist, in press.
DOI: https://doi.org/10.2138/am-2022-8017. http://www.minsocam.org/

Fig.5

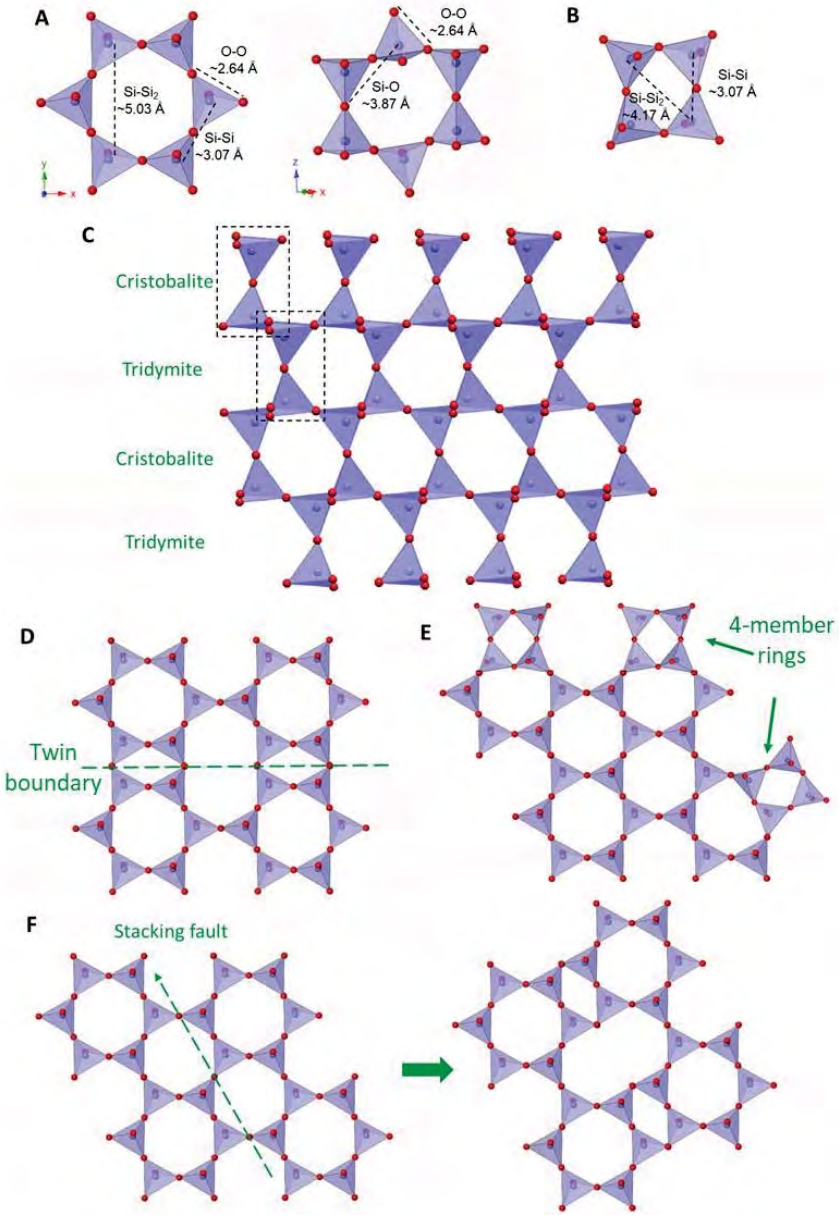

This is the peer-reviewed, final accepted version for American Mineralogist, published by the Mineralogical Society of America.
The published version is subject to change. Cite as Authors (Year) Title. American Mineralogist, in press.
DOI: https://doi.org/10.2138/am-2022-8017. http://www.minsocam.org/

Fig.6

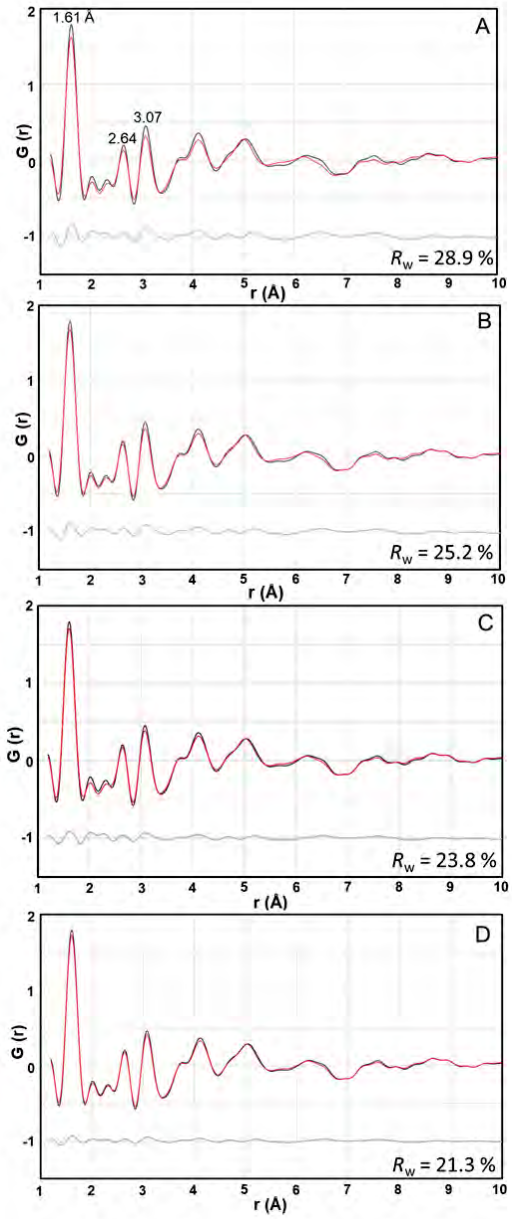

This is the peer-reviewed, final accepted version for American Mineralogist, published by the Mineralogical Society of America.
The published version is subject to change. Cite as Authors (Year) Title. American Mineralogist, in press.
DOI: https://doi.org/10.2138/am-2022-8017. http://www.minsocam.org/

Fig.7